

Single Channel SAR Deception Jamming Suppression via Dynamic Aperture Processing

Bo Zhao, *Member, IEEE*, Lei Huang, *Senior Member, IEEE*, and Jihong Zhang

Abstract—This paper proposed a novel algorithm to suppress the deception jamming against the single channel synthetic aperture radar (SAR), which provides an effective and economic way to improve the anti-deception-jamming ability of the conventional SAR system. The dynamic apertures are employed to provide multiple observations about the time-frequency distributions of the deception jamming and real echoes. The amplitude loss in different dynamic apertures is modeled to formulate the optimization problem for deception jamming suppressing. Super-resolution scheme is also involved to tighten the feasible region of the problem. The effectiveness of the proposed algorithm is verified by simulation.

Index Terms—Synthetic aperture radar (SAR), deception jamming suppression, dynamic aperture.

I. INTRODUCTION

THE synthetic aperture radar (SAR), which has been widely applied to both military and civilian fields, is an efficient approach to remote sensing. With the development of the theory and technology, the game between the SAR and jammer never stops. The deception jamming interrupts the SAR with fine modulated false targets to confuse the information acquisition. Much effort has been done to improve the coverage range, efficiency, accuracy and fidelity of deception jamming [1]–[4]. Its high concealment and low power requirement make it a popular research direction.

At the same time, many anti-deception-jamming methods are developing. Deception jamming cancellation methods based on dual-aperture antenna SAR [5] has been studied. Furthermore, more complex multiple channels/statics are also involved to improve the anti-jamming abilities [6], [7]. Such a system, which usually works silently, provides more degrees of spatial freedom that can hardly be noticed and tackled by the jammer. However, the deployment of multi-channel/static SAR usually results in higher cost than the single channel SAR, which might prevent its implementations in practice.

Manuscript received October 24, 2016; revised March 19, 2017; accepted April 11, 2017. Date of publication April 18, 2017; date of current version June 12, 2017. This work was supported in part by the National Natural Science Foundation of China under Grant U1501253, Grant 61501485, and Grant 61501300, in part by the China Postdoctoral Science Foundation under Grant 2015M582413, in part by the Natural Science foundation of Guangdong Province, China, under Grant 2015A030311030, in part by the Foundation of Shenzhen City under Grant ZDSYS201507081625213, Grant JCYJ20150324140036835, and Grant JCYJ20160520165659418, in part by the Foundation of Nanshan District Shenzhen City under Grant KC2015ZDYF0023A, and in part by the Shenzhen University under Grant 201557. The associate editor coordinating the review of this paper and approving it for publication was Prof. Bernhard Jakoby. (*Corresponding author: Lei Huang*.)

The authors are with the College of Information Engineering, Shenzhen University, Shenzhen 518060, China (email: dr.lei.huang@ieee.org).

Digital Object Identifier 10.1109/JSEN.2017.2695001

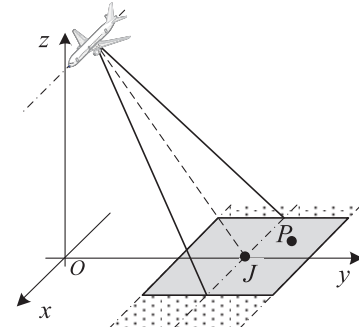


Fig. 1. Geometrical model of SAR imaging and deception jamming.

Based on the defect that the jamming can hardly be modulated within one pulse repetition period (PRI), agile waveform [8], [9] provides a much cheaper anti-jamming solution than the multi-channel/statisc schemes. The quantization error can also be utilized for jamming suppression [10]. However, these methods will fall into the competition circle as the efficiency and accuracy of deception jamming keep improving, which leads to high and endless updating expenses.

Owing to the foregoing reasons, we proposed a novel scheme to suppress the deception jamming against the single channel SAR without incurring additional hardware updating expenses. The dynamic apertures are used to provide multiple observations about the different distributions of the deception jamming and real SAR echo in time-frequency domain. Formulated as an optimization problem, the deception jamming is effectively suppressed and thus the performance does not degrade as the jammer or the SAR system improves.

II. GEOMETRICAL AND SIGNAL MODEL

The geometrical model of SAR imaging and deception jamming is shown in Fig. 1. The zero slow time is set at the moment when the SAR beam center is pointing at the jammer. The axis x is parallel to the track along which the SAR flies, axis z is perpendicular to the ground, axis y is determined by the right-hand rule.

The support region of an arbitrary scatterer, say point P for instance, is $[-T/2 + \tau, T/2 + \tau]$, where T is the synthetic aperture time and τ is the moment when the SAR beam center is pointing at P . The main lobe illuminating area (the dark area in Fig. 1) moves with the SAR at a constant velocity v , thus echoes from different scatterers are gathered.

To insert a false scatterer P' which is imaged the same as the real scatterer P does, the slant range difference $\Delta R'(t_a)$ between the jammer and desired false scatterer is calculated. Utilizing $\Delta R'(t_a)$, the time delay and phase of the intercepted

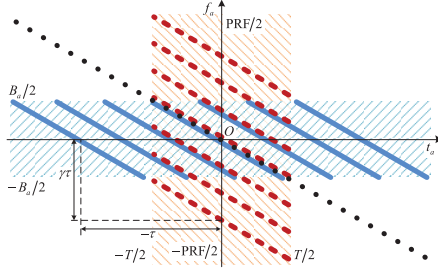


Fig. 2. Time-frequency distribution of the real echoes and deception jamming. signal are modulated by the jammer to generate deception jamming.

$$\begin{aligned} s'_P(t_a) &= \frac{\sigma'_P}{\sigma_J} s_J(t_a) * \delta\left(t_r - \frac{2\Delta R'(t_a)}{c}\right) \\ &\times \exp\left(-j\frac{4\pi}{\lambda}\Delta R'(t_a)\right), \end{aligned} \quad (1)$$

where $*$ is the convolution operator, $\delta(\cdot)$ is the Dirac delta function, σ'_P and σ_J denote the scattering coefficients of the false scatterer and jammer, t_r is the fast time, t_a is the slow time, λ is the wavelength, c is the velocity of light, $s_J(t_a)$ is the intercepted SAR signal, $\Delta R'(t_a) = R(t_a - \tau) - R_J(t_a)$ with $R(t_a - \tau)$ and $R_J(t_a)$ being the slant ranges of the scatterer P and jammer J , respectively. The support region of t_a here is $[-T/2, T/2]$, because the deception jammer usually interrupts the SAR from its main lobe, whose power is conventionally much higher than that in the side lobe to suppress the signal from undesired directions. By doing this, the necessary jamming power is reduced. The characteristic of P in the support region $[-T/2 + \tau, T/2 + \tau]$, which does not totally overlap on that of the jammer, is extended in $[-T/2, T/2]$ to generate a false scatterer. After azimuth coherent processing, both the real echoes and deception jamming can be focused in the image domain with similar resolutions. However, their characteristics in the time-frequency domain vary due to the different formation mechanisms. The relationship between the real echo and deception jamming is given as

$$\begin{aligned} s'_P(t_a) &= s_P(t_a) * \delta(t_a + \tau) \\ &\times \exp(-j\pi\tau(2f_{dc} - \gamma\tau + \gamma t_a)), \end{aligned} \quad (2)$$

where f_{dc} is the Doppler frequency center (if any) and γ is the Doppler chirp rate. They are determined by the first- and second-order terms of the instantaneous slant range, respectively [11]. Denoting the Doppler spectrum of $s_P(t_a)$ by $S_P(f_a)$, we have

$$\begin{aligned} S'_P(f_a) &= S_P(f_a - \gamma\tau) \exp(j2\pi f_a \tau) \\ &\times \exp(-j\pi(2f_{dc}\tau - \gamma\tau^2)). \end{aligned} \quad (3)$$

Compared with $S_P(f_a)$, the false spectrum $S'_P(f_a)$ is shifted along both the Doppler frequency and the slow time axes by $\gamma\tau$ and $-\tau$, respectively. The last exponent term shows up as a constant for a certain τ . The time-frequency distribution is illustrated in Fig. 2.

Although the real echoes of different scatterers distribute in different slow time support regions, their Doppler frequency

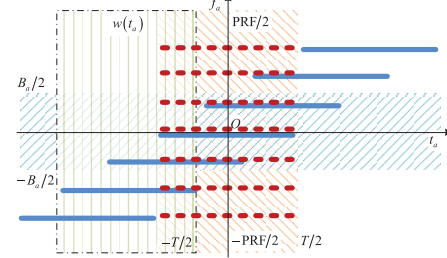


Fig. 3. Time-frequency distribution of the dechirped signal.

characteristics are the same, which lead to a B_a width support region distributing along the slow time axis as the thick solid lines show. Due to the main lobe jamming limitation, the deception jammings lie between $-T/2$ and $T/2$ along the Doppler frequency axis, which are denoted by the thick dashed lines. The support regions of the real echoes and deception jamming totally overlap on each other only when the real and false scatterers lie in the same azimuth cell as the jammer does. The farther a scatterer is away from the jammer in azimuth, the less public region the real echo and the deception jamming share. Basing on the different time-frequency characteristics, a novel scheme based on dynamic apertures is proposed to suppress the deception jamming.

III. DYNAMIC APERTURE PROCESSING

A. Dynamic Aperture Model

For deception jamming suppression purpose, the characteristics of all the real and false scatterers need to be reserved through imaging processing. The dechirp method, which can be illustrated easily and clearly, is employed here for azimuth imaging.

Meanwhile, the Doppler frequency center correction is also performed together with dechirping. Therefore, the reference signal is given as

$$s_0(t_a) = \exp\left(-j\pi(2f_{dc}t_a + \gamma t_a^2)\right). \quad (4)$$

The time-frequency distribution of (4) is shown by the dotted line in Fig. 2. It covers the entire region in which the real echoes and the deception jamming distribute. By performing dechirp on the mixed data with the reference signal, the time-frequency distribution in Fig. 3 is obtained.

The frequency differences between the received signal and reference signal are reserved after dechirping. Being related to the locations of the scatterers, the frequency differences can be projected to the Doppler frequency axis to obtain the azimuth image. Although the slow time domain support regions differ, the deception jamming possesses the same frequency differences as the real echo does. This leads to the same imaging results, and this is also the reason why deception jamming works.

The dynamic aperture $w(t_a)$ is a sliding area surrounded by the dash-dotted line in Fig. 3. It is a data selecting window in the slow time domain, whose expression is

$$\begin{aligned} w(t_a) &= \text{rect}\left(\frac{t_a - \eta}{T}\right) \\ &= \begin{cases} 1, & t_a \in [-T/2 + \eta, T/2 + \eta] \\ 0, & \text{otherwise}, \end{cases} \end{aligned} \quad (5)$$

where η determines the center of the dynamic aperture.

B. Bandwidth Loss Effect

The real echo after dechirping is

$$s_{Pd}(t_a) = \sigma_P a_a(t_a - \tau) \exp(-j2\pi\gamma\tau t_a) \times \exp\left(-j\pi\left(\frac{4R_0}{\lambda} + 2f_{dc}\tau - \gamma\tau^2\right)\right), \quad (6)$$

and the dechirped deception jamming is

$$s'_{Pd}(t_a) = \sigma'_P a_a(t_a) \exp(-j2\pi\gamma\tau t_a) \times \exp\left(-j\pi\left(\frac{4R_0}{\lambda} + 2f_{dc}\tau - \gamma\tau^2\right)\right), \quad (7)$$

where R_0 is the constant component of $R(t_a)$. The coherent gain in range has been ignored. Notice that the difference between (6) and (7) is the support region determined by $a_a(\cdot)$, which can also be seen from Fig. 3. By multiplying $w(t_a)$ to $s_{Pd}(t_a)$ and performing Fourier transform on it, we have

$$\begin{aligned} u(f_a, \eta) &= \mathcal{F}(w(t_a)s_{Pd}(t_a)) = \sigma_P \exp(j\phi) \\ &\quad \mathcal{F}\left(\text{rect}\left(\frac{t_a - (\eta + \tau)/2}{T - |\eta - \tau|}\right) \exp(j2\pi\gamma\tau t_a)\right) \\ &= \alpha(\eta)\sigma_P T \exp(j\phi) \text{sinc}(\alpha(\eta)T(f_a + \gamma\tau)) \\ &\quad \times \exp(-j\pi(f_a + \gamma\tau)(\eta + \tau)), \end{aligned} \quad (8)$$

where \mathcal{F} is the Fourier transformation, $\phi = -\pi(4R_0/\lambda + 2f_{dc}\tau - \gamma\tau^2)$, α is a scaling coefficient describing the amplitude loss and main lobe expanding caused by the motion of the dynamic aperture, given as

$$\alpha(\eta) = \begin{cases} 1 - \frac{|\eta - \tau|}{T}, & \eta \in [-T/2 + \tau, T/2 + \tau] \\ 0, & \text{otherwise.} \end{cases} \quad (9)$$

In all the dynamic apertures, the scatterer P can be focused on the same place, say $-\gamma\tau$. But in different dynamic apertures, its amplitude losses and main lobe expansions are different. With different values of η , different dynamic apertures are formed, and different azimuth profiles, $u(f_a, \eta)$, are obtained.

With the similar derivation, the azimuth profile of the false scatterer can be denoted as

$$\begin{aligned} u'(f_a, \eta) &= \beta(\eta)\sigma'_P T \exp(j\phi) \\ &\quad \times \text{sinc}(\beta(\eta)T(f_a + \gamma\tau)) \\ &\quad \times \exp(-j\pi(f_a + \gamma\tau)\eta), \end{aligned} \quad (10)$$

where the scaling coefficient of the false scatterer is

$$\beta(\eta) = \begin{cases} 1 - \frac{|\eta|}{T}, & \eta \in [-T/2, T/2] \\ 0, & \text{otherwise.} \end{cases} \quad (11)$$

Notice that β does not vary with τ , which means that the false scatterers in the same dynamic aperture have the same amplitude losses and main lobe expansions. Therefore, the different presentations of the real and false scatterers in different dynamic apertures can be utilized for deception jamming suppression.

Denote $u(t_a)$ in the vector form by $\mathbf{u}_w \in \mathbb{C}^{1 \times N}$, where N is the sampling number of the dynamic aperture.

TABLE I
SAR PARAMETERS

Parameter	Value
Bandwidth	300 MHz
Pulse Width	$0.5 \mu\text{s}$
Chirp Rate	$6 \times 10^{14} \text{ Hz/s}$
Wavelength	0.03 m
Aperture Length	1 m
Beamwidth	0.03 rad
Closest Range	10 km
Speed	150 m/s
Squint Angle	0°
Doppler Bandwidth	300 Hz
Synthetic Aperture Time	2 s

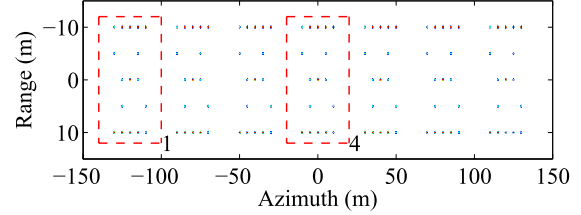


Fig. 4. Mixed image

Employing different dynamic apertures, an observation matrix $\mathbf{U} = [\mathbf{u}_1, \dots, \mathbf{u}_w, \dots, \mathbf{u}_W]^T \in \mathbb{C}^{W \times N}$ is obtained.

According to (8) and (10), the variations of the real and false scatterers can be described by $\mathbf{A}, \mathbf{B} \in \mathbb{C}^{W \times N}$, respectively. Their entries are $a_{w,n} = \alpha_n(\eta)$ and $b_{w,n} = \beta_n(\eta)$, respectively.

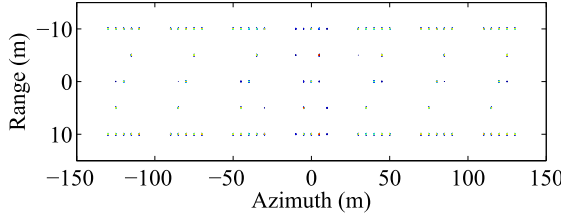
The false targets are usually designed with strong scattering properties to guarantee the effective coverage, which results in the sparsity in the image domain. The main lobe expansion enhances the interaction between scatterers and weakens the sparsity. Therefore, the sparsity and sparse positions of the scatterers are pre-estimated via super-resolution [12]–[15] to simplify the deception jamming suppression problem. Denote the set of the estimated sparse position by $D_t = \{t | \tau_t \in D_p \text{ or } \tau_t \in D_q\}$, where D_p and D_q are the sets of the real and false targets' locations. Then the deception jamming suppression problem can be described as

$$\begin{aligned} \min_{\mathbf{P}, \mathbf{Q}} \quad & \|\mathbf{U} - \mathbf{AP} - \mathbf{BQ}\|_2^2 \\ \text{s.t.} \quad & p_t = q_t = 0, t \in D - D_t, \end{aligned} \quad (12)$$

where $D = [1, N]$ is the complete set for all possible location indexes of a target, $\mathbf{P} = \text{diag}(\mathbf{p})$ and $\mathbf{Q} = \text{diag}(\mathbf{q})$ with $\mathbf{p}, \mathbf{q} \in \mathbb{C}^{1 \times N}$ being the azimuth profiles of the real and false targets, respectively. The sparse position estimation tightens the feasible region of the problem. By using the convex optimization toolbox [16], the real and false targets can be reconstructed, respectively.

IV. SIMULATION

The simulation parameters are shown in Table I. According to the parameters, the azimuth resolution is $\rho = 0.5\text{m}$. The jammer locates at the origin. Seven targets, which are 5×5 scatterers matrix with 5m gaps, say 10ρ , between scatterers in azimuth, distribute evenly to cover the whole synthetic aperture. The real targets are set as Z's, while the false targets are S's. The real and false targets overlap partly on each other. Fig. 4 shows the jammed SAR imaging result.



(a)

(b)

Fig. 5. Deception jamming suppression results. (a) The real scene image. (b) The false scene image.

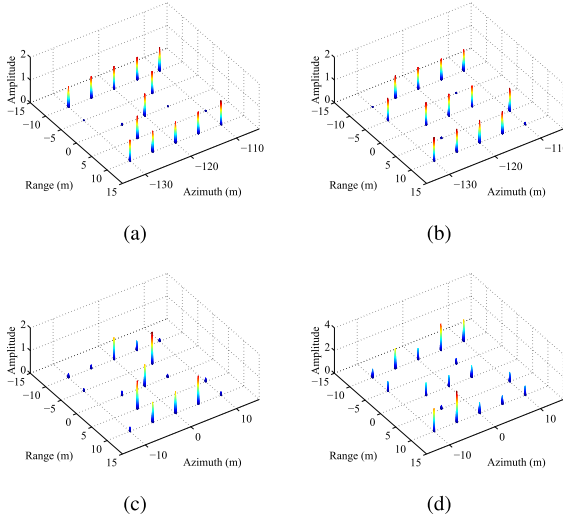
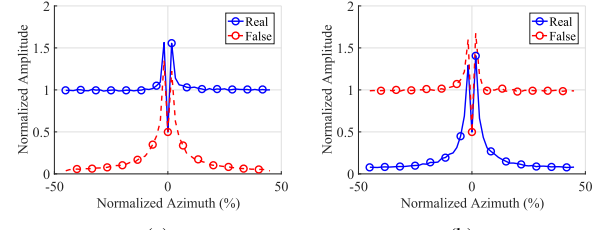


Fig. 6. Detailed images of the targets. (a) Real target 1. (b) False target 1. (c) Real target 4. (d) False target 4.

After accurate modulation, the false targets achieve the similar imaging quality as the real targets do, which make it hard to distinguish them from each other in the image domain. By applying the proposed algorithm, the real and false targets are separated as Fig. 5 shows.

In Fig. 5(a), the Z-shaped real targets are reconstructed. The farther a real target lies away from the jammer, the more similar its time-frequency is to the false target, and the harder it is to be separated. Therefore, the false (real) target residues in the reconstruction result of the real (false) target. Targets 1 and 4, which are circled by the dashed lines in Fig. 4, are further presented to show the details.

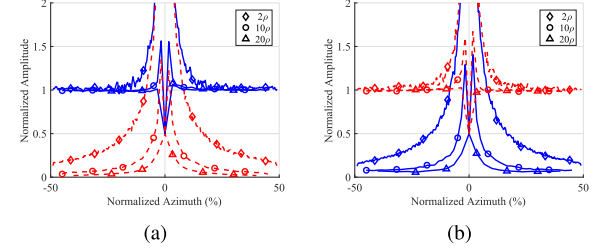
At the edge of the synthetic aperture, the differences of time-frequency characteristics between the real echoes and deception jamming are remarkable. Therefore, both the real and false targets can be reconstructed with high quality, as Figs. 6(a) and (b) show. The scatterers, which show up in



(a)

(b)

Fig. 7. Reconstruction performance. (a) Real targets reconstruction and false targets suppression results. (b) Real targets suppression and false targets reconstruction results.



(a)

(b)

Fig. 8. Reconstruction results with different gaps between scatterers. (a) Real targets reconstruction and false targets suppression results. (b) Real targets suppression and false targets reconstruction results.

both the real and false targets, are separately reconstructed in both of the images. The other scatterers, which belong to only one of the targets, are reconstructed in one image and suppressed in the other one. In Figs. 6(c) and (d), the targets lies beside the jammer cannot be well separated because their time-frequency distributions are too similar.

In Fig. 7, the performance of the proposed scheme is shown through 300 Monte Carlo experiments. In Fig. 7(a), most of the real targets (solid line marked by o's) can be effectively reconstructed while the false ones (dashed line marked by o's) are suppressed. Denote the length of the synthetic aperture by L . When the distance between the scatterers and jammer is smaller than $\pm 3\%L$, more than 20% errors are introduced to the reconstructed amplitudes because the components of the deception jamming are also considered as the real echo. This area is defined as a failure area for reconstruction. The suppression result also decreases between $-10\%L$ to $10\%L$, which is defined as a failure area for suppression. Outside this area, more than 80% energy of the deception jamming can be effectively suppressed. Fig. 7(b) shows the result of the false targets reconstruction while the real ones are suppressed. A similar performance of reconstruction and suppression can be achieved.

1) *Reconstruction Results With Different Gaps*: When the gaps between scatterers get larger, the interaction between scatterers weakens and better reconstruction as well as suppression results can be achieved as Fig. 8 shows. As the gaps between adjacent scatterers increase to 20ρ , the results marked by Δ 's are obtained. Curves obtained using 10ρ -gaped scatterers are also plotted and marked by o's for comparison.

With larger gaps between scatterers, better reconstructions are obtained, and lower energy is retained for the suppressed

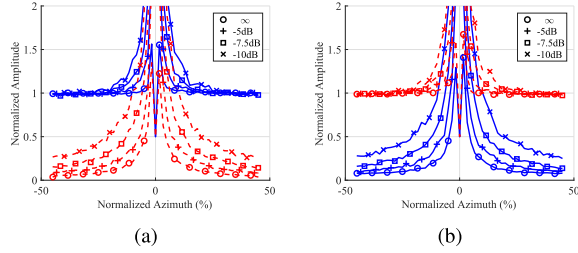


Fig. 9. Reconstruction results with different SNRs. (a) Real targets reconstruction and false targets suppression results. (b) Real targets suppression and false targets reconstruction results.

scatterers. However, the scatterers lying near the jammer (about $\pm 3\%L$) still cannot be well reconstructed. When the gaps get as small as 2ρ (marked by \diamond 's), the reconstruction results become worse. As a result, the reconstruction failure area increases to $\pm 15\%L$. The residual suppressed energy is larger than 20% throughout the synthetic aperture.

2) Reconstruction Results With Different Signal-to-Noise Ratios: Noise is another factor affecting the deception jamming suppression performance. Possessing high coherent processing gains in both range and azimuth domains, SAR and deception jamming have a certain degree of tolerance to noise. As the noise increases, performance of the proposed scheme degrades as Figs. 9 (a) and (b) show.

Simulations for 10ρ -gaped scatterers are performed with different signal-to-noise ratios (SNR). The noise-free cases, say $\text{SNR} = \infty$, are marked by o's for comparison. When $\text{SNR} = -5\text{dB}$, scatterers in $\pm 6\%L$ beside the jammer cannot be effectively reconstructed, and more than 20% energy cannot be suppressed in $\pm 20\%L$. As SNR decreases to -7.5dB , the failure areas for reconstruction and suppression increase to $\pm 10\%L$ and $\pm 30\%L$, respectively (shown by curves marked by \square 's). A -10dB SNR leads to failure of suppression through the whole synthetic aperture. Within $\pm 12\%L$, however, reconstruction errors are smaller than 20% as the curves marked by \times 's show.

Generally, the interactions between adjacent scatterers and the noise degrade the reconstruction performance near the jammer and increase the suppression residual throughout the whole jamming area. Developing efficient approaches to tackle the issue of performance degradation in reconstruction will be our future work.

V. CONCLUSION

This paper proposed a novel algorithm to suppress the deception jamming against single channel SAR. The dynamic apertures are employed to construct the observation matrix about the deception jamming and the real echoes. In this way, the deception jamming suppression can be modeled as an optimization problem to reconstruct the real and false targets, respectively. Simulations for scatterers with different gaps and different SNRs are given to show the performance and limitation of the proposed algorithm. As the future work, the interaction between the adjacent scatterers will be considered to improve the jamming suppression performance.

REFERENCES

- [1] F. Zhou, B. Zhao, M. Tao, X. Bai, B. Chen, and G. Sun, "A large scene deceptive jamming method for space-borne SAR," *IEEE Trans. Geosci. Remote Sens.*, vol. 51, no. 8, pp. 4486–4495, Aug. 2013.
- [2] B. Zhao, F. Zhou, and Z. Bao, "Deception jamming for squint SAR based on multiple receivers," *IEEE J. Sel. Topics Appl. Earth Observ. Remote Sens.*, vol. 8, no. 8, pp. 3988–3998, Aug. 2015.
- [3] Z. Bo, F. Zhou, X. Shi, Q. Wu, and B. Zheng, "Multiple targets deception jamming against ISAR using electromagnetic properties," *IEEE Sensors J.*, vol. 15, no. 4, pp. 2031–2038, Apr. 2015.
- [4] Y. Liu, W. Wang, X. Pan, Q. Fu, and G. Wang, "Inverse omega-K algorithm for the electromagnetic deception of synthetic aperture radar," *IEEE J. Sel. Topics Appl. Earth Observ. Remote Sens.*, vol. 9, no. 7, pp. 3037–3049, Jul. 2016.
- [5] C. Li and D. Zhu, "The detection of deception jamming against SAR based on dual-aperture antenna cross-track interferometry," in *Proc. Int. Conf. Radar*, Oct. 2006, pp. 1–4.
- [6] W. Xiong, G. Zhang, F. Wen, Y. Zhang, and J. Yin, "Trilinear decomposition-based spatial-polarisation filter method for deception jamming suppression of radar," *IET Radar Sonar Navigat.*, vol. 10, no. 4, pp. 765–773, 2016.
- [7] S. Zhao, N. Liu, L. Zhang, Y. Zhou, and Q. Li, "Discrimination of deception targets in multistatic radar based on clustering analysis," *IEEE Sensors J.*, vol. 16, no. 8, pp. 2500–2508, Apr. 2016.
- [8] M. Soumekh, "SAR-ECCM using phase-perturbed LFM chirp signals and DRFM repeat jammer penalization," *IEEE Trans. Aerosp. Electron. Syst.*, vol. 42, no. 1, pp. 191–205, Jan. 2006.
- [9] M. A. Hossain, I. Elshafiey, M. A. Alkanhal, and A. Mabrouk, "Anti-jamming capabilities of UWB-OFDM SAR," in *Proc. Eur. Radar Conf. (EuRAD)*, Oct. 2011, pp. 313–316.
- [10] S. C. Luo, "An algorithm of deception jamming suppression based on blind signal separation," *J. Electron. Inf. Technol.*, vol. 33, no. 12, pp. 167–170, 2011.
- [11] I. G. Cumming and H. C. Wong, "Digital processing of synthetic aperture radar data: Algorithms and implementation," in *Proc. Int. Radar Conf.*, 1980, pp. 168–175.
- [12] C. He, L. Liu, L. Xu, M. Liu, and M. Liao, "Learning based compressed sensing for SAR image super-resolution," *IEEE J. Sel. Topics Appl. Earth Observ. Remote Sens.*, vol. 5, no. 4, pp. 1272–1281, Aug. 2012.
- [13] F. Biondi, "Compressed sensing radar—New concepts of incoherent continuous wave transmissions," in *Proc. CoSeRa*, Jun. 2015, pp. 204–208.
- [14] J. Tsao and B. D. Steinberg, "Reduction of sidelobe and speckle artifacts in microwave imaging: The CLEAN technique," *IEEE Trans. Antennas Propag.*, vol. 36, no. 4, pp. 543–556, Apr. 1988.
- [15] Z. Bi, J. Li, and Z.-S. Liu, "Super resolution SAR imaging via parametric spectral estimation methods," *IEEE Trans. Aerosp. Electron. Syst.*, vol. 35, no. 1, pp. 267–281, Jan. 1999.
- [16] M. Grant and S. Boyd. (Mar. 2014). *CVX: Matlab Software for Disciplined Convex Programming*, Version 2.1. [Online]. Available: <http://cvxr.com/cvx>



Bo Zhao (M'15) was born in Henan, China, in 1986. He received the B.Sc. and Ph.D. degrees from Xidian University, Xi'an, China, in 2010 and 2015, respectively.

He is currently a Post-Doctoral Researcher with the Institute of Multi-Dimensional Signal Processing, Shenzhen University. His research interests include radar imaging, SAR countermeasure, and compressive sensing.



Lei Huang (M'07–SM'14) was born in Guangdong, China. He received the B.Sc., M.Sc., and Ph.D. degrees in electronic engineering from Xidian University, Xi'an, China, in 2000, 2003, and 2005, respectively.

From 2005 to 2006, he was a Research Associate with the Department of Electrical and Computer Engineering, Duke University, Durham, NC, USA. From 2009 to 2010, he was a Research Fellow with the Department of Electronic Engineering, City University of Hong Kong, and a Research Associate with the Department of Electronic Engineering, Chinese University of Hong Kong. From 2011 to 2014, he was a Professor with the Department of Electronic and Information Engineering, Harbin Institute of Technology Shenzhen Graduate School. Since 2014, he has been with the Department of Information Engineering, Shenzhen University, where he is currently a Distinguished Professor. His research interests include spectral estimation, array signal processing, statistical signal processing, and their applications in radar, and navigation and wireless communications.

He is currently serving as an Associate Editor of the IEEE TRANSACTIONS ON SIGNAL PROCESSING and *Digital Signal Processing*. Additionally, he is an Elected Member in the Sensor Array and Multichannel Technical Committee of the IEEE Signal Processing Society.



Jihong Zhang was born in Jiangsu, China, in 1964. He received the B.Eng., M.Eng., and Ph.D. degrees from Southeast University, Nanjing, China, in 1986, 1989, and 1992, respectively.

From 1995 to 1996, he was a Visiting Scholar with the University of Central Lancashire, U.K. In 1997, he was a Visiting Scholar with Soka University, Japan. In 2000, he was a Visiting Scholar with the University of Liverpool, U.K. He is a Professor with the College of Information Engineering, Shenzhen University. His research interests include digital signal processing, artificial neural network, fuzzy logic, ant colony optimization and their applications in wireless communications and video/image/speech processing.